Engineering Science & Technology
https://ojs.wiserpub.com/index.php/EST/

UNIVERSAL WISER PUBLISHER

Research Article

Reduced-Order Models Correlating Ti Beta 21S Microstructures and Vickers Hardness Measurements

Mostafa Mahdavi[1], Mike Standish[1], Almambet Iskakov[2], Hamid Garmestani[1], Surya R. Kalidindi[2,3*]

[1]School of Materials Science and Engineering, Georgia Institute of Technology, Atlanta, GA, 30332, USA
[2]George W. Woodruff School of Mechanical Engineering, Georgia Institute of Technology, Atlanta, GA, 30332, USA
[3]School of Computational Science and Engineering, Georgia Institute of Technology, Atlanta, GA, 30332, USA
E-mail: surya.kalidindi@me.gatech.edu

Received: 24 August 2020; **Revised:** 12 December 2020; **Accepted:** 14 December 2020

Abstract: Ti Beta 21S alloy is a metastable titanium beta alloy commonly used in the aerospace industry, especially in jet engines. Components made from this alloy are usually subjected to various thermal histories during service, which leads to significant changes in their microstructures and associated mechanical properties. The central goal of this study is to demonstrate the feasibility of correlating the optical images of the microstructure obtained from heat-treated samples of Ti Beta 21S to their respective Vickers hardness measurements. This is achieved using recently established analyses and statistical quantification approaches based on the principal components of the rotationally invariant 2-point spatial correlations. The correlations extracted in this work can be used for non-destructive diagnostics of in-service components.

Keywords: Vickers hardness, Ti Beta 21S alloy, thermal treatments, structure-property linkage

1. Introduction

A fundamental tenet of the field of materials science and engineering is that the material internal structure (i.e., microstructure) controls its effective mechanical properties [1]-[7]. Indeed, a large number of prior experimental and modeling studies have explored microstructure-property linkages in various material classes [8]-[14]. The present study is focused on metal alloys employed in structural applications. Optical microscopy has served as one of the most commonly employed low-cost approaches for experimentally documenting the microstructures in metal alloys. While optical microscopy can successfully reveal the mesoscale grain and phase structure of the alloy, it is incapable of providing information on the chemical composition. Similarly, hardness measurements have served as one of the most commonly employed low-cost approaches for assessing the resistance to plastic deformation in a metal alloy. Given that these techniques are widely used by the metal industry, it raises an obvious question-is it possible to establish reliable correlations between the optical micrographs and hardness measurements in a selected metal alloy system? Obviously, any such correlations would have to be confined to a prescribed alloy composition, as variations in the composition cannot be inferred from the optical micrographs. Therefore, the main variable to be considered in such correlations would be the different heat treatments that might be applied to the alloy, which induce corresponding changes in the microstructure. Furthermore, such explorations are also unlikely to capture the effects of cold work on the microstructure as changes in dislocation densities cannot be inferred reliably from the optical micrographs. In this

DOI: https://doi.org/10.37256/est.4220233136

paper, we examine critically the viability of establishing reliable quantitative correlations between optical micrographs and hardness measurements in a heat-treatable alloy.

Several previous studies have explored the relationship between the microstructure and composition of materials and their hardness measurements. Rajakumar et al. [15] modeled the relationship between grain size and hardness of the weld nugget of friction-stir-welded AA6061-T6 aluminum alloy using a linear relationship that exhibited a coefficient of determination (R^2) of 79.2%. The low fidelity of this model indicates that there are other microstructural parameters that control the mechanical properties that need to be considered in order to arrive at a higher fidelity model. In another study, Heidarzadeh et al. [16] used the Hall-Petch equation to correlate hardness to the grain size for friction-stir-welded Cu-Zn alloys and found that microstructural inhomogeneities contributed significantly to the loss of fidelity of the models. The central challenge in such studies comes from the need to incorporate higher-order descriptors of microstructure that go beyond the highly simplified descriptors such as the volume fraction of each phase or the average particle size.

Recently, Kalidindi and co-workers have introduced the Materials Knowledge Systems (MKS) framework for capturing the correlations between microstructures and the properties associated with them using emergent data science tools [17], [18]. One of the key advantages of MKS lies in its use of a comprehensive set of microstructure descriptors. In this paper, we used this framework for quantifying the optical micrographs obtained from differently heat-treated samples of Ti Beta 21S alloy and establishing correlations to their measured hardness values. The heat treatments employed covered a temperature range of 350-750 °C, while the heat treatment times were in the range of 10 minutes to 24 hours. Ti Beta 21S exhibits diverse two-phase microstructures in these ranges of heat treatments along with a wide range of mechanical properties [19]-[21]. Consequently, this metal serves as a good candidate for the present study.

2. Materials and sample preparation

Generally, pure titanium exists as a hexagonal close-packed (hcp) α-phase and can transform into a body center cubic (bcc) β-phase at an elevated temperature [22]. Ti Beta 21S (Ti-15Mo-3Nb-3Al-0.2Si) is a metastable β-phase (bcc) material produced for the aircraft industry due to its high oxidation and corrosion resistance [23]. This material can transform into a two-phase ($\alpha + \beta$) microstructure when aged below β-transus temperature (807 °C), as secondary α-phase particles nucleate [24].

In this study, two sheets of 1.054 mm thick TIMET TIMETAL® 21S (Ti-15Mo-3Nb-3Al-0.2Si, ASTM Grade 21) provided by Boeing Company, Huntsville, AL, USA, were cut into pieces with dimensions of 127 × 203 mm. Samples were put in the furnace at a pre-set temperature and then removed at different time points. The full matrix of heat treatments applied covered temperatures between 350 °C to 750 °C with 50 °C steps (9 different temperatures) and aging times of 10 minutes, 30 minutes, 2 hours, 5 hours, and 24 hours (a total of five different aging times). Not every specimen in the matrix was included in the study, as some samples did not exhibit detectable α-phase nucleation. Since our focus is on relating the α-β morphology in the optical micrographs to their hardness values, single-phase samples do not offer useful data for the present study. The heat treatments for the 20 samples chosen for the study are identified in Table 1 below. When removed from the oven, samples were quenched immediately in water to preserve the microstructure corresponding to each thermal treatment. The samples were then mounted using a Struers CitoPress-1 in phenol and methenamine based conductive material called Konductomet® purchased from Buehler Company, Lake Bluff, IL, USA. The mounting press was set for a four-minute heat cycle at 180 °C followed by a six-minute cooling cycle at a pressure of 4,200 psi. All titanium cutting operations were done prior to aging with an ISOMET® 1000 diamond saw to ensure clean cuts. The mounted samples were polished using a Struers RotoPol-31 automatic polisher equipped with a RotoForce-4 wheel head and multidose. During polishing, six samples were sequentially ground from 240 grit paper down to a soft pad with a colloidal silicon suspension in order to achieve a mirror finish. Samples were exposed to fifteen minutes of ultrasonication in water, followed by rinsing with methanol to remove excess silicon on the surface of the samples. Samples were etched using an oxalic etch (490 mL oxalic acid, 10 mL Hydrogen Fluoride (HF)) and Kroll's reagent (435 mL water, 60 mL nitric acid, 5 mL HF). Residual etchant on the mounting material was neutralized using a baking soda solution before rinsing with water and methanol. A Zeiss optical microscope was used to take images of each sample under different magnifications (200X, 500X, and 1,000X) in order to document each sample's microstructure.

3. Results and discussion

3.1 *Optical micrographs and Vickers hardness measurements*

Optical micrographs were taken at the magnification of 200X for each sample (20 images in total). Figure 1(a)-(c) shows three of the optical micrographs, representing the variety of microstructures observed in the samples studied in this work. In Figure 1, the darker colored regions represent α-phase and the lighter colored regions represent β-phase. As seen in Figure 1(a), α-phase is more prevalent in the sample aged well below the β-transus temperature of 807 °C. For a moderately high temperature such as 550 °C (see Figure 1(b)), the α-phase is less prevalent. The trend continues at 700 °C (see Figure 1(c)), where we see a clear dominance of the β-phase. Also, some of the darkly colored features in Figure 1 appear at grain boundaries. These regions were analyzed using back-scattered electrons in the Scanning Electron Microscope (SEM) to ensure that they represent α-phase regions (see Figure 1(b) and (c)). From the images acquired, it is clear that the α and β phases exhibit very different phase morphology and spatial distributions after the application of the different treatments explored in this study. The grain sizes in these samples varied from about 2 microns to around 40 microns.

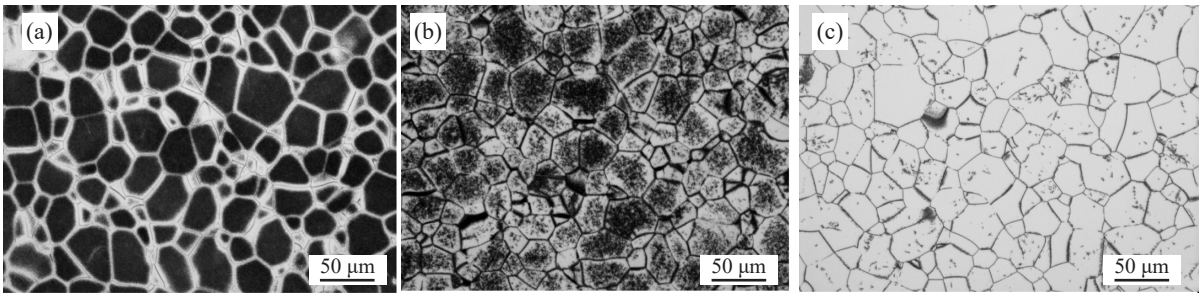

Figure 1. Example optical microscopy images of Ti Beta 21S taken from samples subjected to three thermal treatments: a) 450 °C for 2 hrs, b) 550 °C for 30 min, and c) 700 °C for 30 min

After optical microscopy, Vickers hardness was measured on all the samples using a Leco hardness machine using a fixed load of 2 kg. At least five different measurements were made in each sample.

Table 1 summarizes the measured Vickers hardness values for each microstructure included in this study. Additionally, Figure 2 illustrates the dependence of the measured Vickers hardness values on the aging time and temperature as a contour map. The minimum and maximum hardness values corresponded to the sample aged at 650 °C for 10 min with a hardness of 281.34 ± 5.9 (HV) and the sample aged at 500 °C for 5 hrs with a hardness of 436.86 ± 3.3 (HV), respectively. The large difference in the hardness demonstrates that this alloy can be hardened significantly by aging.

Table 1. The average and standard deviations of the Vickers hardness measurements for at least five tests in each aged sample. A total of twenty different aging treatments were employed in this study

Sample	350 °C 2 hrs	350 °C 5 hrs	350 °C 24 hrs	400 °C 5 hrs	400 °C 24 hrs	450 °C 10 min	450 °C 2 hrs	450 °C 5 hrs	500 °C 2 hrs	500 °C 5 hrs
Vickers hardness (HV)	291.0 ± 2.1	290.8 ± 2.7	396.5 ±2.7	385.4 ± 4.7	399.8 ± 2.6	286.5 ± 4.9	355.1 ± 1.9	381.2 ± 2.9	375.3 ± 3.4	436.6 ± 3.3
Sample	550 °C 30 min	600 °C 10 min	600 °C 30 min	650 °C 10 min	650 °C 2 hrs	700 °C 30 min	700 °C 2 hrs	750 °C 10 min	750 °C 2 hrs	750 °C 5 hrs
Vickers hardness (HV)	326.1 ± 4.2	389.2 ± 3.1	394.6 ± 5.1	281.3 ± 5.9	359.3 ± 3.5	297.7 ± 4.1	338.6 ± 2.2	297.9 ± 3.4	292.9 ± 3.1	294.1 ± 4.9

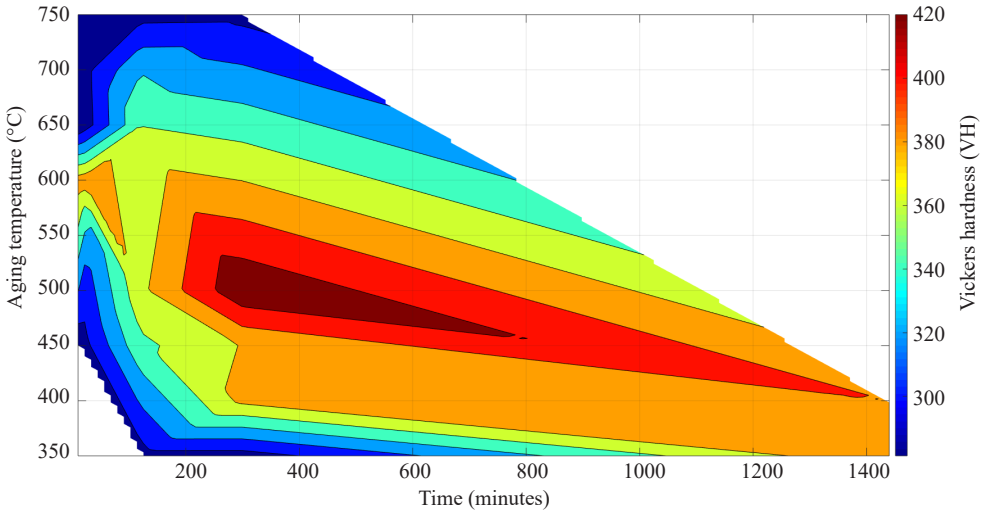

Figure 2. The contour map of the Vickers hardness data presented in Table 1

The micrographs obtained in this study were segmented using a suite of image processing techniques such as thresholding, edge detection, and smoothing. Image segmentation is an important step in this study, as the structure quantification (needed for establishing the structure-property linkage) is performed on the segmented micrographs. Two strategies were explored to ensure that we capture all of the important features in the segmented micrographs. The first strategy was to compare the segmented versions of the micrographs taken at a magnification of 200X with the corresponding ones taken at a higher magnification image of 1,000X to ensure that the small features (i.e., phase regions) in the images are correctly captured. The second strategy used was to overlay the segmented and raw images on top of each other to check the segmentation results around the grain boundaries (paying specific attention to the width and connectivity of grain boundaries). Figure 3(a)-(c) shows the segmented versions of the images shown in Figure 1(a)-(c).

3.2 *Microstructure quantification*

In this study, the microstructure statistics are obtained using the framework of 2-point spatial correlations (also called 2-point statistics) defined as [25]

$$f_r^{hh'} = \frac{1}{S_r} \Sigma_{s=1}^{S} m_s^h m_{s+r}^{h'} \tag{1}$$

where s = 1, 2, ..., S indexes all of the pixels in the micrograph, h indexes the distinct local states (here it indexes the two thermodynamic phases present in the micrographs), m_s^h is the volume fraction of local state h in pixel s, and $f_r^{hh'}$ captures the joint probability of finding the local state h at the tail and the local state h' at the head of the vector r placed randomly in the microstructure. Compared to the highly simplified statistical measures of the microstructure such as the phase volume fractions and average grain size, 2-point statistics provide a rigorous and comprehensive set of statistical measures of the microstructure [26]. For example, the zero vector (r is equal to zero) in the autocorrelation of local state h, denotes the volume fraction of the local state h. Additionally, information of size and shape distributions of the local state are embedded in the 2-point statistics [26]. Another salient aspect of the 2-point statistics is that it automatically captures anisotropy in the microstructure statistics. For a microstructure with two local states, only one of the autocorrelations is independent (e.g., [27]). In the present study, we have computed and used the autocorrelations of the β-phase (colored white in the segmented images in Figure 3(a)-(c)). Figure 3(d)-(f) presents the 2-point statistics maps for the autocorrelation of the β-phase for the segmented images shown in Figure 3(a)-(c). As already mentioned, the center peaks in these autocorrelation maps capture the β-volume fractions, while the contours close to the central peak embed information on size and shape distributions of the β-phase. The three-segmented images shown in Figure 3(a)-(c) depict mostly isotropic distributions with decreasing sizes of the β-phase regions, respectively. The autocorrelation

maps indicate that the scan size is much larger than the coherence lengths seen in these autocorrelation maps. Coherence length reflects the microstructural length scale where the autocorrelations asymptote to a value equal to the square of the volume fraction [1], indicating that the spatial placement of the β-pixels is uncorrelated beyond this length scale. For the images shown in Figure 3(a)-(c), the coherence lengths are seen to be around 1-2 times the average size of the β-regions, indicating that their spatial placement in the microstructure is quite random. Since all of the segmented images used in this study employed the exact same resolution in terms of the pixel size, the autocorrelation maps also exhibit a consistent spatial resolution. Given the relatively short coherence lengths observed in the images, the autocorrelation maps were truncated to keep only the vector components below 50 μm, as shown in Figure 3(d)-(f).

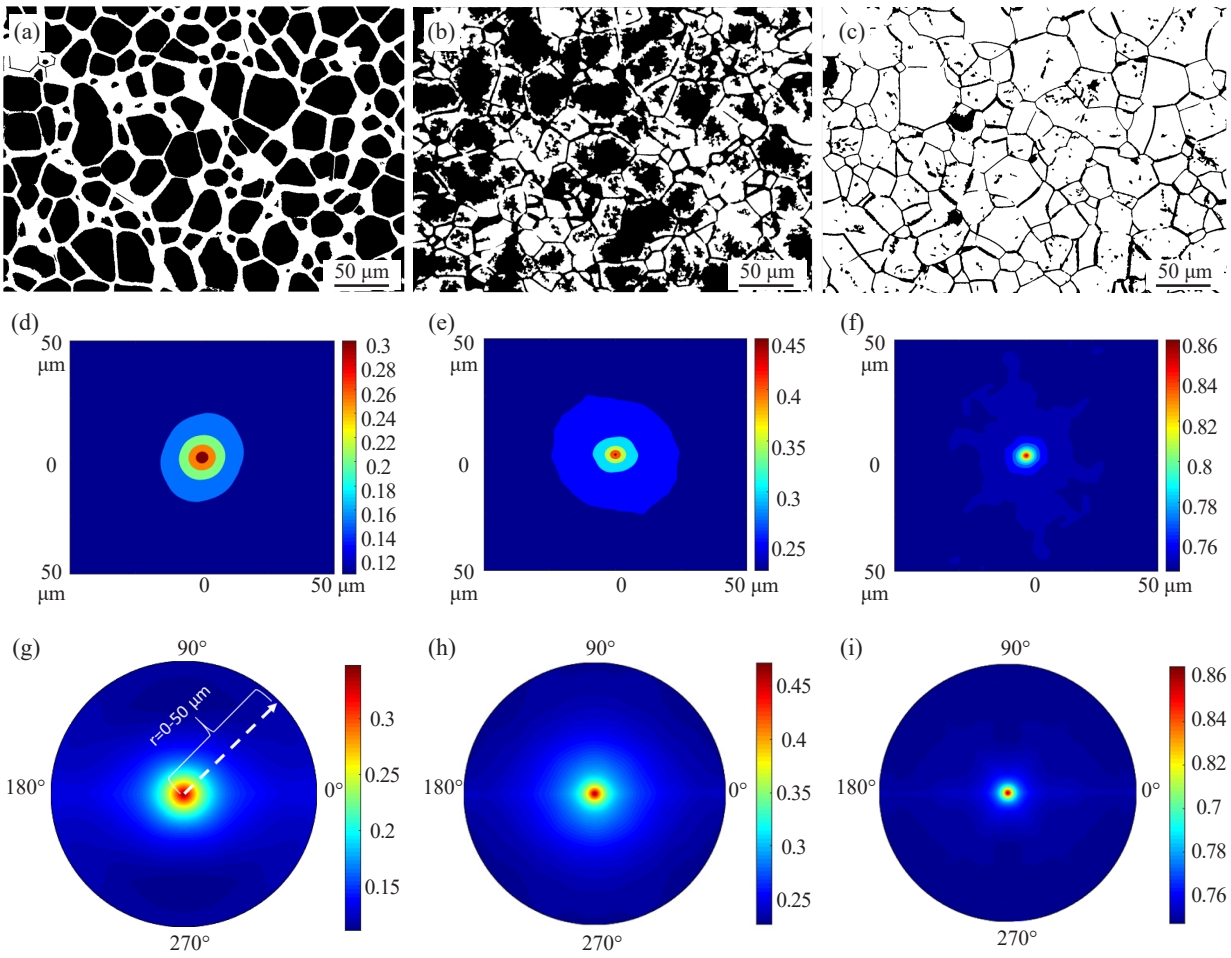

Figure 3. Segmented example micrographs from three samples aged at (a) 450 °C for 2 hrs, (b) 550 °C for 30 min, and (c) 700 °C for 30 min. The darker regions in these images correspond to the α-phase, while the lighter regions correspond to β-phase. (d)-(f) Autocorrelations of β-phase corresponding to the segmented images shown in (a)-(c). (g)-(i) RI2SS maps corresponding to the segmented images shown in (a)-(c)

One of the challenges in using the autocorrelations shown in Figure 3(d)-(f) is that they are sensitive to the selection of the observer reference frame. In other words, rotation of the images would result in a corresponding rotation of the autocorrelation maps. Therefore, if the images do not have a clearly specified natural reference frame, this causes a problem in comparing the statistics obtained from the different samples. In order to overcome this challenge, Cecen et al. [28] have recently introduced a rotationally invariant version of the 2-point statistics called RI2SS (rotationally invariant 2-point statistics). RI2SS filters out the effects of the observer reference frame while retaining the inherent anisotropic structural information. This is accomplished by first expressing the 2-point statistics in polar coordinates, applying a Discrete Fourier Transform (DFT) only on the angular dimension, removing the phase angle information,

and computing an inverse DFT to recover RI2SS in polar coordinates. Figure 3(g)-(i) shows the RI2SS plots for the 2-point autocorrelations shown in Figure 3(d)-(f). The removal of the phase angle information shifts the dominant phase information to θ = 0°. In other words, the horizontal line connecting θ = 0° to θ = 180° in Figure 3(g)-(i) represents Pair Correlation Function (PCF) or radial distribution function (RDF) [1], [29], [30], which reflect directionally averaged 2-point spatial correlations in the image. It has been shown that the RI2SS retains information about the relative anisotropy in the spatial correlations in the image that are independent of the observer reference frame. Figure 3(g)-(i) shows that the images exhibit mostly isotropic spatial correlations with only faint hints of anisotropy at short length scales (i.e., 20-40 μm). It is important to understand that a substantially large scan is needed to reliably capture the autocorrelations presented in Figure 3. Indeed, in the present study, it was seen that the spatial correlations attained consistent and reliable values when the scan size (430 μm × 300 μm) was increased to over 15 times the typical feature size (i.e., the size of the beta region).

3.3 *Principal component analysis*

The RI2SS maps shown in Figure 3(g)-(i) result in a high-dimensional vector of descriptors for every microstructure. Specifically, each RI2SS map shown in these figures includes 400 radial bins and 180 circumferential bins (using one-degree bins and using only one half by taking advantage of symmetry in these maps), resulting in a total of 400 × 180 = 72,000 microstructure statistics for each sample. This result is an extremely high dimensional representation of the microstructure statistics. In prior work, it was demonstrated that Principal Component Analysis (PCA) can be utilized to obtain an objective (i.e., data-driven) low-dimensional representation of the microstructure statistics [14] that have been found to be especially well suited for formulating reduced-order Process-Structure-Property (PSP) linkages [14]. Mathematically, these low-dimensional representations of the RI2SS can be expressed as

$$f^{(k)} \approx \sum_{i=1}^{R} \alpha_i^{(k)} \varphi_i + \bar{f} \tag{2}$$

where $f^{(k)}$ represents a vectorized set of RI2SS for the microstructure labeled (k), and α_i, φ_i, and $\bar{f}$ denote the principal component (PC) scores, the PC basis, and the ensemble average of all the vectorized RI2SS for the complete set of 20 images included in this study. The accuracy of the representation in Eq. (2) is controlled by the truncation level in the number of retained PCs, R. Since PCA organizes the PCs such that they systematically capture the highest amount of variance in the dataset, the expansion in Eq. (2) is naturally convergent. For the micrographs analyzed in this work, the ensemble average statistics ($\tilde{f}$) and the first two PC basis maps (φ_1 and φ_2) are shown in Figure 4. The basis maps identify a normalized weighted set of spatial statistics that are systematically increased (or decreased) in the microstructure as the corresponding PC score increases (or decreases). All of the changes captured by each PC score are always in relation to the ensemble average ($\tilde{f}$).

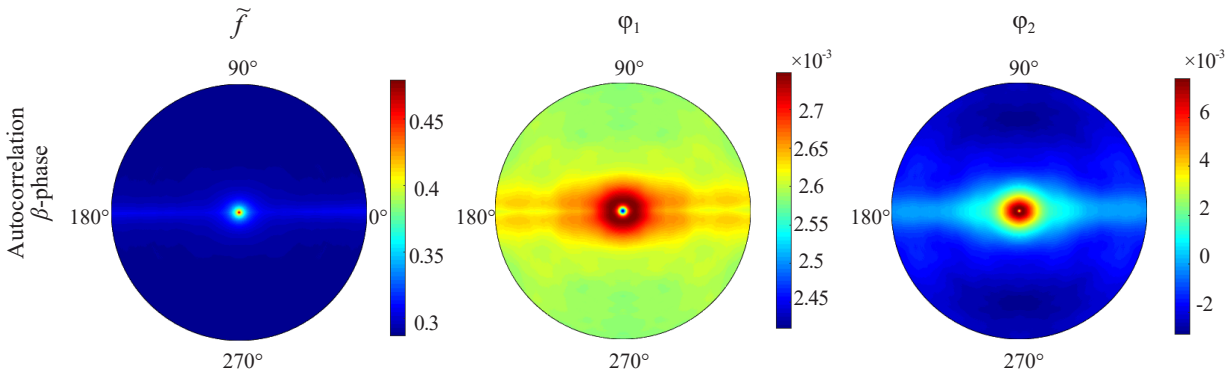

Figure 4. Representation of the ensemble average and the first two PC basis maps

In order to interpret and understand the PC representations obtained from Eq. (2), it is useful to examine the ensemble of microstructure statistics aggregated in the subspace corresponding to the first few PCs. Figure 5 shows the PC1-PC2 representations of the RI2SS for all samples used in this study. In prior studies [14], [25], it was generally observed that PC1 is highly correlated to the phase volume fraction information. This should not be interpreted that PC1 carries information only on the volume fractions. In fact, it is quite clear from the PC basis maps shown in Figure 4 that PC1 is not exclusively correlated with the phase volume fraction. This is because the value at the center of these basis maps corresponds to the value of the phase volume fraction and the observation that the values at the center of the higher-order PC basis maps (i.e., PC2 and higher) are not zero.

The microstructures studied in this work covered a roughly triangular region in the PC1-PC2 space, as shown in Figure 5. As expected, it is seen that PC1 scores correlated well with the β-phase volume fractions. Also as expected, the PC representations presented similar micrographs closer together based completely on the RI2SS computed from the micrographs, without the specification of any other information (such as the beta volume fractions or average feature sizes). This is clearly seen by noting that the three "corners" of the triangular region seen in Figure 5 corresponds to distinctly different microstructure morphologies. The left corner of the microstructure space in Figure 5 is populated with micrographs with low β-volume fractions, and with beta occupying mainly the grain boundary regions around equiaxed α. As one moves to the right in the microstructure space, one clearly sees an increase in the β-volume fractions. However, the microstructures in the top right and bottom right of the microstructure space are distinctly different, even though they exhibit similar β-volume fractions. In other words, PC1 score is significantly more correlated with β-volume fraction, compared to the PC2 score. The main differences between the top and bottom microstructures on the right side are actually in the morphology of α, with equiaxed α at the top and mostly grain boundary α at the bottom. Although the PCA was performed on the autocorrelations of the β, it implicitly contains information on the morphology of α. It is seen that PCA effectively organized the microstructure space shown in Figure 5 based on the differences in their RI2SS. PCA also revealed that the first two PCs account for 99.97% of the variance in the complete ensemble of micrographs employed in this study. Indeed, it is remarkable that only a handful of PCs are required to represent the complex material structure seen in the diverse set of micrographs. This special feature has been the central characteristic in multiple other formulations of highly accurate PSP linkages obtained using the MKS framework [14], [18], [31].

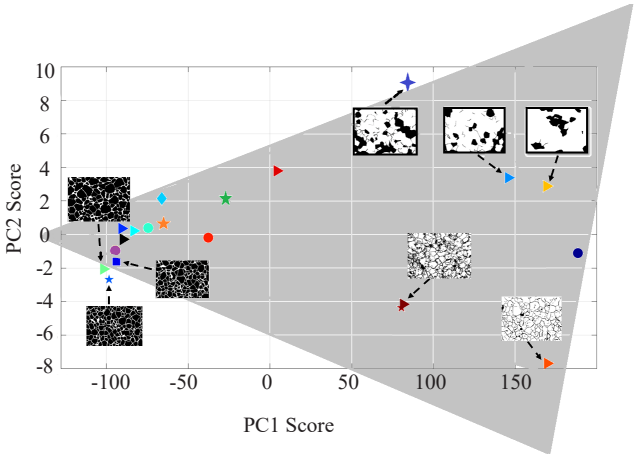

Figure 5. PC1-PC2 representations of the RI2SS for all samples used in this study along with corresponding micrographs for selected points

3.4 *Structure-property linkages*

Building on prior work [14], [32], we next extract a model that takes the PC scores of RI2SS as inputs and predicts their hardness as the output. Since the first two PC scores captured about 99.97% of the total variance in the dataset gathered for this work, only the first two PC scores were used to build the desired model. There exist a large number of options for model building that range from regression techniques [33], [34] to neural networks [35], [36] to non-

parametric approaches such as Gaussian process regression (GPR) [37], [38]. Neural networks typically require a large dataset and therefore were not deemed suitable for the present study. Given the relatively small dataset available for the present study (a total of 20 data points), it was decided to explore standard (least-squares) regression using a polynomial model form. In this work, the inputs were considered as the first two PC scores (i.e., PC1 and PC2 values), while the output was considered as the hardness measured from the sample.

The performances of the models built (for different orders of polynomials) in this work were critically compared against each other using the cross-validation technique. In the cross-validation technique employed here, for each attempt at building the model, three microstructures were randomly selected for the test set and the rest (17 microstructures) were used as the training set. The entire process was repeated eight times for each model. The errors on all of the test data points are then collected, resulting in a total of 24 errors. The following definition of the percentage error was employed in these computations:

$$E^{(k)} = \left(\frac{\left|H^{(k)} - H^{*(k)}\right|}{H^{(k)}}\right)100 \tag{3}$$

where $H^{(k)}$ is the measured Vickers hardness of i^{th} microstructure and $H^{*(k)}$ is the predicted Vickers hardness in each validation test. From the aggregated set of 24 errors, we have computed an average error and a standard deviation of the test errors. These were used as measures of the accuracy and robustness of the model. For building a regression model, a simple polynomial model between the microstructure features (i.e., PC scores) and the target (i.e., hardness value) was explored. This polynomial model can be expressed as

$$H^{*} = X\beta + \varepsilon \tag{4}$$

where X denotes various monomials of the PC scores and β is a set of unknown parameters. As an example, for a second-order polynomial with the first two PC scores, the monomials considered would include 1, α_1, α_2, $\alpha_1\alpha_2$, α_1^2, and α_2^2. The model parameters (β) are established using Ordinary Least Squares (OLS) estimation as

$$\beta = (X^T X)^{-1} X^T H \tag{5}$$

Models of different polynomial orders with the first two PC scores were explored in this study. Although the inclusion of more features (i.e., more of the monomials) usually produces a lower error value in the training, it often also results in higher cross-validation errors for the test data points (indicating an over-fit of the model). This is especially the case in the present study because of the small number of data points (i.e., only 20 micrographs). To find the best model, different combinations of inputs (i.e., features) among PC1, $PC1^2$, $PC1^3$, PC2, $PC2^2$, $PC2^3$, $PC1 \times PC2$, $PC1^2 \times PC2$, $PC1 \times PC2^2$, and $(PC1 \times PC2)^2$ were utilized. In total, 45 models were explored, and cross-validation was used to identify the best surrogate model. Table 2 summarizes the best five models built in this work based on the cross-validation errors.

Table 2. Cross-validation errors for the five best models built in this work using different features selected from the monomials of the PC scores representing the microstructure

Monomials in the regression	Average error for cross-validation technique
PC1, PC2, $PC1^2$, $PC1 \times PC2$, $PC1 \times PC2^2$	3.15%
PC1, PC2, $PC1^2$, $PC2^2$, $PC1 \times PC2$	8.10%
PC1, PC2, $PC1^2$, $PC1 \times PC2$	10.23%
PC1, PC2, $PC2^2$, $PC1 \times PC2$	13.72%
PC1, PC2, $PC1^2$, $PC1^3$, $(PC1 \times PC2)^2$	17.41%

The best model (with the lowest cross-validation error) obtained in our trials is expressed as:

$$H^i = 0.0293(PC1 \times PC2) - 3.2038(PC2) + 0.0021(PC1 \times PC2^2) - 0.5938(PC1) + 0.0024(PC1)^2 + 315.9711 \quad (6)$$

It should be noted that the cross-validation error for the best model was significantly lower compared to the second-best model, suggesting that the inputs used for the best model are indeed significantly more important. The very low cross-validation error indicates that we do not have an overfit for our model. The cross-validation errors for the best model from Table 2 are presented in a parity plot in Figure 6. In this study, due to the limited dataset, a polynomial model was used with a convex optimization method. If a large dataset was available, neural networks [39] might offer a better alternative. This is because neural networks allow for learning a much larger class of functions. These methods offer various computational efficiencies in dealing with large data sets [40].

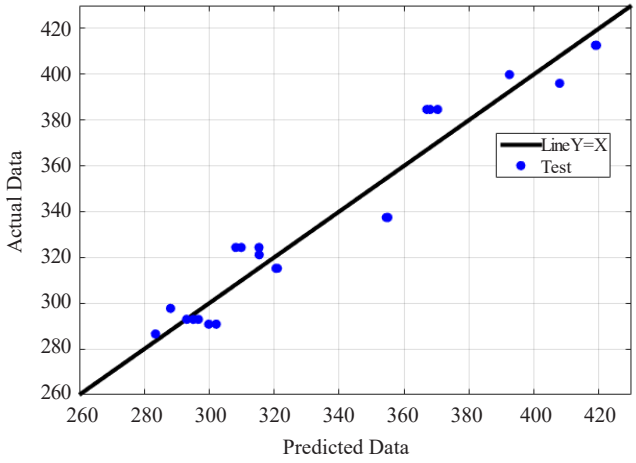

Figure 6. The cross-validation predictions of structure-property linkage for the model shown in Eq. (6)

It should be noted that only 20 different structures have been used in this study. Therefore, it is expected that the structure-property linkage will change when new data points are added. However, as more data points are added, the structure-property linkage developed by the approach presented in this work is expected to stabilize. This is because similar structure-property linkages extracted from data simulation generated from micromechanical finite element models have already been shown to exhibit this trend [41]. The strength of this strategy is that the model can be allowed to improve as more data becomes available, possibly from multiple research groups.

4. Conclusion

In this study, we measured Vickers hardness on samples of Ti Beta 21S alloy after different thermal treatments. These measurements were successfully correlated to the corresponding microstructures in the samples obtained using optical micrographs. This was accomplished using the first two principal components of the rotationally invariants 2-point autocorrelations as the microstructure features. It was observed a simple polynomial model developed using these features produced a surrogate model with a cross-validation error of about 3%. This opens up new research avenues for establishing valuable structure-property linkages in metal samples using high throughput experimental protocols and the emerging data science toolsets.

Acknowledgments

Mostafa Mahdavi and Hamid Garmestani appreciate the support from the Boeing Company. Almambet Iskakov and Surya Kalidindi acknowledge support from ONR N00014-18-1-2879. Their all support is highly appreciated.

Conflict of interest

The authors declare no competing financial interest.

References

[1] S. Torquato, *Random Heterogeneous Materials: Microstructure and Macroscopic Properties*, Springer Science & Business Media, 2013.
[2] B. L. Adams and T. Olson, "The mesostructure-properties linkage in polycrystals," *Progress in Materials Science*, vol. 43, no. 1, pp. 1-87, 1998.
[3] J. D. Eshelby, "The determination of the elastic field of an ellipsoidal inclusion, and related problems," *Proceedings of the Royal Society of London Series A Mathematical and Physical Sciences*, vol. 241, no. 1226, pp. 376-396, 1957.
[4] M. Mahdavi, E. Hoar, D. E. Sievers, Y. Chong, N. Tsuji, S. Liang, and H. Garmestani, "Statistical representation of the microstructure and strength for a two-phase Ti-6Al-4V," *Materials Science and Engineering: A*, vol. 759, pp. 313-319, 2019.
[5] F. Monteverde, S. Guicciardi, and A. Bellosi, "Advances in microstructure and mechanical properties of zirconium diboride based ceramics," *Materials Science and Engineering: A*, vol. 346, no. 1-2, pp. 310-319, 2003.
[6] T. Watanabe and S. Tsurekawa. "The control of brittleness and development of desirable mechanical properties in polycrystalline systems by grain boundary engineering," *Acta Materialia*, vol. 47, no. 15-16, pp. 4171-4185, 1999.
[7] E. Chlebus, K. Gruber, B. Kuźnicka, J. Kurzac, and T. Kurzynowski, "Effect of heat treatment on the microstructure and mechanical properties of Inconel 718 processed by selective laser melting," *Materials Science and Engineering: A*, vol. 639, pp. 647-655, 2015.
[8] S. Y. Han, S. Y. Shin, S. Lee, N. J. Kim, J. H. Kwak, and K. G. Chin, "Effect of carbon content on cracking phenomenon occurring during cold rolling of three light-weight steel plates," *Metallurgical and Materials Transactions A*, vol. 42, no. 1, pp. 138-146, 2011.
[9] P. Kusakin, A. Belyakov, C. Haase, R. Kaibyshev, and D. A. Molodov, "Microstructure evolution and strengthening mechanisms of Fe-23Mn-0.3 C-1.5 Al TWIP steel during cold rolling," *Materials Science and Engineering: A*, vol. 617, pp. 52-60, 2014.
[10] H. E. Sabzi, A. Z. Hanzaki, H. Abedi, R. Soltani, A. Mateo, and J. Roa, "The effects of bimodal grain size distributions on the work hardening behavior of a TRansformation-TWinning induced plasticity steel," *Materials Science and Engineering: A*, vol. 678, pp. 23-32, 2016.
[11] G. B. Olson, "Computational design of hierarchically structured materials," *Science*, vol. 277, no. 5330, pp. 1237-1242, 1997.
[12] K. Rajan, *Informatics for Materials Science and Engineering: Data-Driven Discovery for Accelerated Experimentation and Application*, British: Butterworth-Heinemann, 2013.
[13] B. S. Fromm, K. Chang, D. L. McDowell, L-Q. Chen, and H. Garmestani, "Linking phase-field and finite-element modeling for process-structure-property relations of a Ni-base superalloy," *Acta Materialia*, vol. 60, no. 17, pp. 5984-5999, 2012.
[14] A. Gupta, A. Cecen, S. Goyal, A. K. Singh, and S. R. Kalidindi, "Structure-property linkages using a data science approach: Application to a non-metallic inclusion/steel composite system," *Acta Materialia*, vol. 91, pp. 239-254, 2015.
[15] S. Rajakumar, C. Muralidharan, and V. Balasubramanian, "Statistical analysis to predict grain size and hardness of the weld nugget of friction-stir-welded AA6061-T 6 aluminium alloy joints," *The International Journal of Advanced Manufacturing Technology*, vol. 57, no. 1-4, pp. 151-165, 2011.
[16] A. Heidarzadeh and T. Saeid, "Correlation between process parameters, grain size and hardness of friction-stir-welded Cu-Zn alloys," *Rare Metals*, vol. 37, no. 5, pp. 388-398, 2018.
[17] S. R. Kalidindi, S. R. Niezgoda, G. Landi, S. Vachhani, and T. Fast, "A novel framework for building materials

knowledge systems," *Computers, Materials, & Continua*, vol. 17, no. 2, pp. 103-125, 2010.
[18] T. Fast, S. R. Niezgoda, and S. R. Kalidindi, "A new framework for computationally efficient structure-structure evolution linkages to facilitate high-fidelity scale bridging in multi-scale materials models," *Acta Materialia*, vol. 59, no. 2, pp. 699-707, 2011.
[19] P. J. Bania, "Next generation titanium alloys for elevated temperature service," *ISIJ International*, vol. 31, no. 8, pp. 840-847, 1991.
[20] J. Williams, "Kinetics and phase transformations (in Ti alloys)," *Titanium Science and Technology*, pp. 1433-1494, 1973.
[21] K. Chaudhuri and J. Perepezko, "Microstructural study of the titanium alloy Ti-15Mo-2.7 Nb-3Al-0.2 Si (TIMETAL 21S)," *Metallurgical and Materials Transactions A*, vol. 25, no. 6, pp. 1109-1118, 1994.
[22] J. Zhang, C. C. Tasan, M Lai, A-C. Dippel, and D. Raabe, "Complexion-mediated martensitic phase transformation in Titanium," *Nature Communications*, vol. 8, pp. 14210, 2017.
[23] J. D. Cotton, R. D. Briggs, R. R. Boyer, S. Tamirisakandala, P. Russo, N. Shchetnikov, and J. C. Fanning, "State of the art in beta titanium alloys for airframe applications," *Jom*, vol. 67, no. 6, pp. 1281-1303, 2015.
[24] B. Martin, P. Samimi, and P. Collins, "Engineered, spatially varying isothermal holds: Enabling combinatorial studies of temperature effects, as applied to metastable titanium alloy β-21S," *Metallography, Microstructure, and Analysis*, vol. 6, no. 3, pp. 216-220, 2017.
[25] A. Cecen, T. Fast, and S. R. Kalidindi, "Versatile algorithms for the computation of 2-point spatial correlations in quantifying material structure," *Integrating Materials and Manufacturing Innovation*, vol. 5, no. 1, pp. 1, 2016.
[26] B. L. Adams, S. Kalidindi, and D. T. Fullwood, *Microstructure Sensitive Design for Performance Optimization*, British: Butterworth-Heinemann, 2012.
[27] S. Niezgoda, D. Fullwood, and S. Kalidindi, "Delineation of the space of 2-point correlations in a composite material system," *Acta Materialia*, vol. 56, no. 18, pp. 5285-5292, 2008.
[28] A. Cecen, Y. C. Yabansu, and S. R. Kalidindi, "A new framework for rotationally invariant two-point spatial correlations in microstructure datasets," *Acta Materialia*, vol. 158, pp. 53-64, 2018.
[29] A. P. Roberts, "Statistical reconstruction of three-dimensional porous media from two-dimensional images," *Physical Review E*, vol. 56, no. 3. pp. 3203, 1997.
[30] B. Bochenek and R. Pyrz, "Reconstruction of random microstructures-a stochastic optimization problem," *Computational Materials Science*, vol. 31, no. 1-2, pp. 93-112, 2004.
[31] D. B. Brough, D. Wheeler, J. A. Warren, and S. R. Kalidindi, "Microstructure-based knowledge systems for capturing process-structure evolution linkages," *Current Opinion in Solid State and Materials Science*, vol. 21, no. 3, pp. 129-140, 2017.
[32] N. H. Paulson, M. W. Priddy, D. L. McDowell, and S. R. Kalidindi, "Reduced-order structure-property linkages for polycrystalline microstructures based on 2-point statistics," *Acta Materialia*, vol. 129, pp. 428-438, 2017.
[33] C. R. Rao, C. R. Rao, M. Statistiker, C. R. Rao, and C. R. Rao, *Linear Statistical Inference and Its Applications*, New York: John Wiley & Sons, Inc., 1973.
[34] F. Mosteller and J. W. Tukey, *Data Analysis and Regression: A Second Course in Statistics*, Mass.: Addison-Wesley, 1977.
[35] L. K. Hansen and P. Salamon, "Neural network ensembles," *IEEE Transactions on Pattern Analysis & Machine Intelligence*, vol. 12, no. 10, pp. 993-1001, 1990.
[36] D. F. Specht, "A general regression neural network," *IEEE Transactions on Neural Networks*, vol. 2, no. 6, pp. 568-576, 1991.
[37] J. Quiñonero-Candela and C. E. Rasmussen, "A unifying view of sparse approximate Gaussian process regression," *Journal of Machine Learning Research*, vol. 6, pp. 1939-1959, 2005.
[38] C. E. Rasmussen, "Gaussian processes in machine learning," in *Advanced Lectures on Machine Learning. ML 2003. Lecture Notes in Computer Science*, O. Bousquet, U. von Luxburg, and G. Rätsch, Eds. Springer, Berlin, Heidelberg, 2003, pp. 63-71.
[39] A. Cichocki, R. Unbehauen, and R. W. Swiniarski, *Neural Networks for Optimization and Signal Processing*, New York: John Wiley & Sons, Inc., 1993.
[40] W. Ye, C. Chen, Z. Wang, I-H. Chu, and S. P. Ong, "Deep neural networks for accurate predictions of crystal stability," *Nature Communications*, vol. 9, no. 1, pp. 1-6, 2018.
[41] M. I. Latypov, M. Kühbach, I. J. Beyerlein, J-C. Stinville, L. S. Toth, T. M. Pollock, and S. R. Kalidindi, "Application of chord length distributions and principal component analysis for quantification and representation of diverse polycrystalline microstructures," *Materials Characterization*, vol. 145, pp. 671-685, 2018.